Expert Systems With Applications 99 (2018) 168–179

Contents lists available at ScienceDirect

Expert Systems With Applications

journal homepage: www.elsevier.com/locate/eswa

Computer-aided detection and diagnosis of mammographic masses using multi-resolution analysis of oriented tissue patterns

Jayasree Chakraborty[a,*], Abhishek Midya[a], Rinku Rabidas[b]

[a] Department of Surgery, Memorial Sloan Kettering Cancer Center, New York, NY 10065, USA
[b] Department of Electronics and Communication Engineering, National Institute of Technology Silchar, 788010, India

ARTICLE INFO

Article history:
Received 24 August 2017
Revised 8 January 2018
Accepted 9 January 2018
Available online 31 January 2018

Keywords:
Breast cancer
Mammography
Mass detection
Mass classification
Multi-resolution analysis
CADx

ABSTRACT

In this article, a novel approach is proposed for automatic detection and diagnosis of mammographic masses, one of the common signs of non-palpable breast cancer. However, detection and diagnosis of mass are difficult due to its irregular shape, variability in size, and occlusion within breast tissue. The main aim of this study is to classify masses into benign and malignant after detecting them automatically. We propose an iterative method of high-to-low intensity thresholding controlled by radial region growing for the detection of masses. Based on the observation that in presence of mass orientation of tissue patterns changes, which may differ from benign to malignant, a multi resolution analysis of orientation of tissue patterns is then performed to categorize them. The performance of the proposed algorithm is evaluated with images from the digital database for screening mammography (DDSM), containing 450 benign masses, 440 malignant masses, and 410 normal images. A sensitivity of 85.0% is achieved at 1.4 false positives per image in mass detection, whereas an area under the receiver operating characteristic curve of 0.92 with an accuracy of 83.30% is achieved for the diagnosis of malignant masses.

1. Introduction

Being the leading cause of cancer related death among women, breast cancer is one of the major concern for the biomedical researchers. According to International Agency for Research on Cancer, in 2012, approximately 12% of the new cancer cases and 25% of all cancer cases, diagnosed among women, are breast cancer (American Cancer Society, 2015; Ferlay, Soerjomataram, Ervik, Dikshit, Eser, & Mathers, 2013). Its incidence and mortality rates have increased by more than 20% and 14%, respectively, since the estimates of 2008 (Ferlay, Shin, Bray, Forman, Mathers, & Parkin, 2010; 2013). Although no effective technique is developed till now for the prevention of breast cancer, many fold reduction in mortality rate can be achieved among women of all ages by early detection with screening mammography (American Cancer Society, 2015). In spite of its effectiveness, reading mammograms is a challenging task for radiologists due to the subtle nature of mammographic abnormalities, poor image quality, lack of expert radiologists, and fatigue for interpreting large numbers of images in a limited time etc. Computer-based technologies can increase the accuracy of screening by assisting the radiologists as a second reader in the detection and diagnosis of abnormalities of breast cancer (Chakraborty, Rangayyan, Banik, Mukhopadhyay, & Desautels, 2012b; Oliver, Freixenet, Mart, Prez, Pont, & Denton, 2010).

Among different abnormalities, visible in a mammogram, masses are one of the frequent signs of breast cancer. Detection and diagnosis of mass is difficult, due to its variation in shape, size, and margin; especially in the presence of dense breast. Although, a large number of algorithms have been developed to solve these issues, considering them as two independent tasks (Casti, Mencattini, Salmeri, Ancona, Mangeri, & Pepe, 2016), no one can assure full success. Moreover, only a limited studies focused on designing an unified system to detect and diagnose masses, simultaneously (Casti et al., 2016; Casti, Mencattini, Salmeri, Ancona, Mangieri, & Rangayyan, 2014; Tang, Rangayyan, Xu, Naqa, & Yang, 2009). Further researches are required in this direction. A brief overview of different existing techniques is provided in Section 2.

The present study attempts to design an efficient tool for automatic detection and diagnosis of masses in mammogram. Towards this, an iterative method of multilevel high-to-low intensity thresholding nested with radial region growing is applied for the detection of masses (Chakraborty, Mukhopadhyay, Singla, Khandelwal, & Rangayyan, 2012). The application of region growing, after each step of thresholding, restrict uncontrollable growth of candidate mass region and helps to detect a mass occluded within dense tissue, one of the challenge for radiologists. The regions of interests detected as masses are then categorized into benign

* Corresponding author.
E-mail address: chakrabj@mskcc.org (J. Chakraborty).

https://doi.org/10.1016/j.eswa.2018.01.010
0957-4174/

and malignant based on the hypothesis that orientation of tissue patterns changes with malignancy which reflects in mammographic appearance (Chakraborty, Midya, Mukhopadhyay, & Sadhu, 2013). The preliminary study on mass detection was presented in (Chakraborty, Mukhopadhyay, Singla, Khandelwal, & Rangayyan, 2013) and mass classification with manually selected regions of interest (ROIs) was presented in (Midya & Chakraborty, 2015). The designing of a unified system for the detection and diagnosis of masses is the main contribution of this work over (Chakraborty et al., 2013; Midya & Chakraborty, 2015). Moreover, a detailed analysis of the parameters, fine tuning of algorithms, more experimental validation with larger dataset and different combination of features are included in the present study.

The rest of the paper is organized as following. A brief overview of the existing techniques is provided in Section 2. The detailed description of the database followed by proposed mass detection and classification schemes are discussed in Sections 3 and 4, respectively. The performance of the methods is analyzed in Section 5. Finally, Section 6 concludes the paper with a direction for future research.

2. Literature review

Till now many researches have been reported for the detection and diagnosis of masses. However, most of these methods addressed either of them considering as two distinct tasks.

Mass detection methods generally follow hierarchical approach of potential region detection followed by false positive (FP) reduction (Cheng, Shi, Min, Hu, Cai, & Du, 2006; Liu & Zeng, 2015; Oliver et al., 2010; Tang et al., 2009). Some researchers enhanced mass regions in mammogram by designing filters (Kobatake, Murakami, Takeo, & Nawano, 1999; Petrick et al., 1996; Petrick, Chan, & Sahiner, 1999; Varela, Tahoces, Mendez, Souto, & Vidal, 2007) and segmented the regions using thresholding. Considering masses as approximately round convex regions Kobatake et al. (1999) and Varela et al. (2007) applied iris filter to enhance mass-like structures followed by thresholding to segment them. FPs were then reduced employing a neural network classifier with different imaging features and obtained a sensitivity of 88% with 1.02 FPs/image. Based on the hypothesis that masses appear as high-intensity focal regions enclosed by regions with gradually diminishing intensity, multilevel thresholding was widely used for automatic detection of masses in mammograms (Chakraborty et al., 2012; Choi, Kim, & Ro, 2012; Dominguez & Nandi, 2008; Eltonsy, Tourassi, & Elmaghraby, 2007; Gao, Wang, Li., & Tao, 2010; Mudigonda, Rangayyan, & Desautels, 2001; Oliver et al., 2010). Eltonsy et al. (2007) and Gao et al. (2010) proposed multiple concentric layer thresholding to localize the potential sites of masses. Applying multi-resolution LBP on ROIs, obtained with multilevel thresholding, an area under the receiver operating characteristics (ROC) curve (A_z value) of 0.90 was obtained in Choi et al. (2012). These methods are simple yet effective; however, a number of parameters are needed to be optimized. Additionally, masses occluded by dense tissues may be missed by these methods. In a different approach texture proximity mask was generated with micro-genetic algorithm to detect suspicious mass region (de Sampaio, Silva, de Paiva, & Gattass, 2015). The method reported a sensitivity of 92.99% with 0.15 FPs per image after FP reduction using DBSCAN with a proximity ranking and local binary patterns (LBP) with support vector machines (SVM). Mahersia, Boulehmi, and Hamrouni (2016) detected masses with an accuracy of 95.14% by measuring the gaussian density in wavelet domain. Some studies focused on feature extraction and classification for FP reduction with manually selected ROIs (Junior, da Rocha, Gattass, Silva, & de Paiva, 2013; Ramos, do Nascimento, & Pereira, 2012; Reyad, Berbar, & Hussain, 2014; Zyout, Czajkowska, & Grzegorzek, 2015). A technique combining features obtained from LBP, contourlet transform, and discrete wavelet transform (DWT) has been proposed in Reyad et al. (2014). Ramos et al. (2012) detected masses with an A_z value of 0.90 extracting co-occurrence matrix from ridgelet and wavelet transformed images obtained from manually selected ROIs. Tai et al. detected masses using statistical features extracted from gray level co-occurrence matrix (GLCM) and optical density co-occurrence Matrix (ODCM), computed from potential mass region, and achieved an A_z value of 0.98 (Tai, Chen, & Tsai, 2014).

Characterization of masses as benign or malignant is generally performed with manually selected ROI or automatically segmented lesion. Based on the observation that benign masses are well circumscribed, round, or oval in shape with low density and malignant masses are ill-defined, spiculated with high density, many techniques have been reported for the classification of masses based on shape (Gorgel, Sertbas, Kilic, Ucan, & Osman, 2009), margin (Cheng et al., 2006; Rouhi & Jafari, 2016), and texture information (Buciu & Gacsadi, 2011; Cheng et al., 2006; Islam, Ahmadi, & Sid-Ahmed, 2010; Mohanty, Senapati, Beberta, & Lenka, 2013; Pak, Kanan, & Alikhassi, 2015; Rabidas, Midya, & Chakraborty, 2017; da Rocha, Junior, Silva, de Paiva, & Gattass, 2016; Rouhi & Jafari, 2016; Xie, Li, & Ma, 2016). Since the accuracy of shape and margin-based features highly depends on the proper segmentation of masses, texture features are preferably used for mass classification. Among different texture features Haralick's features extracted from GLCM at different regions of masses (Mohanty et al., 2013; Sahiner, Chan, Petrick, Helvie, & Goodsitt, 1998; Tan, Pu, & Zheng, 2014) were widely investigated. Mohanty et al. achieved an accuracy of 96.7% with 170 images from the DDSM database combining GLCM with gray level run length matrix (GLRLM) (Mohanty et al., 2013). An A_z value of 0.78 was obtained with Gabor features extracted at different orientation and frequency while experimented with 322 images (Buciu & Gacsadi, 2011). Xie et al. (2016) obtained an accuracy of 96.02% via segmentation of masses using level set and feature selection by a combination of SVM with extreme learning machine. A content-based image retrieval system along with texture features was introduced by Tsochatzidis, Zagoris, Karahaliou, Costaridou, and Pratikakis (2017) for the classification of benign-malignant masses. Different transformations, such as DWT (Nascimento, Martins, Neves, Ramos, Flores, & Carrijo, 2013), Curvelet (Eltoukhy, Faye, & Samir, 2012), or ripplet (Rabidas, Chakraborty, & Midya, 2017) were also applied for mass categorization. Directional tissue patterns were analyzed by several researchers, such as Chakraborty et al. (2013) and Muramatsu, Hara, Endo, and Fujita (2016) proposed two angle co-occurrence matrices (ACMs) to quantify the angular distribution of orientation of tissue patterns for mass classification and obtained an A_z value of 0.77 with manually selected ROIs of 225 benign and 219 malignant masses.

Although, many methods exist for detection or diagnosis of masses, automatic system for the whole process, as proposed in the present study, is rare (Casti et al., 2016; Mudigonda et al., 2001; Polakowski, Cournoyer, Rogers, DeSimio, Ruck, & Hoffmeister, 1997). Mudigonda et al. (2001) generated iso-intensity contour map using multi-level thresholding for the detection of potential mass regions followed by flow-field and GLCM-based texture analysis for the rejection of FPs and benign-malignant mass classification, respectively. With a dataset of 56 images containing 30 benign, 13 malignant, and 13 normal cases the approach obtained a sensitivity of 81% at 2.2 FPs/image for mass detection and an A_z value of 0.79 for classification. A recent work applied Gaussian curvature and multi-directional Gabor filters to extract suspicious ROI (Casti et al., 2016). A series of two-stage classification was then applied to separate masses from normal tissue using differential features and to identify malignant masses from the others using contour-independent features (Casti et al., 2016).

The method achieved a sensitivity of 0.80 at 5.21 FPs/image for the detection and an A_z value of 0.61 for the diagnosis with a dataset of 785 normal and 877 masses containing 416 malignant cases from the DDSM. However, for clinical use much improvement is required and many challenges are required to be considered (Mazurowski, Lo, Harrawood, & Tourassi, 2009).

3. Materials

The proposed CADx system was evaluated with a set of 1257 randomly selected images from the Digital Database for Screening Mammography (DDSM) collected at the University of South Florida (Heath, Bowyer, Kopans, Moore, & Kegelmeyer, 2001). The dataset contains 450 benign masses, 440 malignant masses, and 410 normal images. The images are with a gray-level resolution of 12 bits/pixel and spatial resolutions of 50 μm/pixel, 43.5 μm/pixel, or 42 μm/pixel. The annotations of masses are available with the database. Two mammographic images, including a benign and a malignant mass, are shown in Fig. 1.

4. Methodology

In the proposed CADx system first we detect mammographic masses using a hybrid method of multi-level thresholding and radial region growing followed by FP reduction. The masses are then diagnosed as benign and malignant using multi-resolution analysis of orientation of tissue patterns of mammogram. Accordingly, the method is divided into the following two sub-sections and schematically diagrammed in Fig. 2.

4.1. Detection of masses

The system level block diagram of the mass detection is shown in the top row of Fig. 2.

4.1.1. Pre-processing

The preprocessing stage consists of the following steps: downsampling of the images by a factor of four in each directions for the reduction of computational complexity, segmentation of breast regions to remove artifacts and the background of images using a previously reported method for breast region segmentation (Ferrari, Rangayyan, Borges, & Frère, 2004).

4.1.2. Partitioning of the breast area

The presence of pectoral muscle may affect the detection of masses in MLO view of mammogram due to their similar intensity. Seldom masses are found within the pectoral muscle region too. Hence, in current study, instead of removal of entire pectoral region, first, the pectoral muscle is detected via a two stage algorithm—approximation of pectoral muscle by a straight line using gradient- and shape-based features, followed by fine tuning using local searching (Chakraborty, Mukhopadhyay, Singla, Khandelwal, & Bhattacharyya, 2011), then the detection of masses are carried in two regions: pectoral muscle region and breast region without pectoral muscle.

4.1.3. Detection of suspicious regions of masses with iterative method of thresholding controlled by region growing

Based on the hypothesis that a mass appears as a high-density space-occupying region with continuous distribution of intensity; a high-intensity central region enclosed by layers of gradually diminishing intensity, an iterative method of high-to-low intensity thresholding is developed. To control the spread of segmented mass region in dense breast we use radial region growing after each stage of thresholding.

a) Detection of focal regions of masses: In this process of multi-level thresholding, we have started from the highest intensity ($\mathbf{I}_{\max}$) as the starting threshold value and continue to reduce the threshold value with a step size of $\delta = \frac{\mathbf{I}_{\max}}{2(L-1)}$, where L is the number of threshold levels. This thresholding process continues till $Th_i = \frac{\mathbf{I}_{\max}}{2}$ as the intensity of mass is generally above 50% of the maximum intensity of the image, where Th_i is the threshold value at the ith iteration.

After ith level of thresholding, let Λ_i be the set of obtained disjoint regions as,

$$\Lambda_i = \left\{ \lambda^k(x,y) |\ \mathbf{I}(x,y) \geq Th_i\ \&\lambda^k \cap \lambda^l = \emptyset \right\}_{k,l=1,2,\cdots,K;k\neq l},$$

where **I(x, y)** is the intensity of the image at pixel position (x, y); K, the number of disjoint regions, is obtained after thresholding the image with the threshold value Th_i. Each of the disjointed areas ($\lambda^k \in \Lambda_i$) must be larger than a disk shaped structural element (Γ) to be considered as potential focal region as given below,

$$\lambda^k \supseteq \Gamma. \tag{1}$$

Let $\tilde{\Lambda}_i$ be the set of potential focal regions, such that

$$\tilde{\Lambda}_i = \left\{ \tilde{\lambda}^j | \lambda^j \in \Lambda_i\ \&\ \lambda^j \supseteq \Gamma \right\}_{j=1,2,\cdots J\leq K}.$$

However, some of the elements of $\tilde{\Lambda}_i$, may be already detected as potential sites of masses during the past levels of thresholding i.e. $\tilde{\Lambda}_i \cap \tilde{\Lambda}_{i-l} \neq \emptyset\ , l = 1, 2, \cdots, i-1$. Hence, the regions processed earlier are rejected to avoid the revisiting of the same region. Finally, we obtain a set of potential focal region of masses Ω_i after the ith iteration for radial region growing as given by,

$$\Omega_i = \left\{ \tilde{\lambda^n} | \tilde{\lambda^n} \in \tilde{\Lambda}_i\ \&\ \tilde{\lambda}^n \notin \Omega_{i-l} \right\}_{n=1,2,\cdots,N\leq J, l=1,2,\cdots,N\leq(i-1)}.$$

After each level of thresholding, a fast radial region growing is applied on each focal region $\lambda \in \Omega_i$ for detecting the potential mass regions.

b) Detection of suspicious regions of masses with coarse boundary: Unlike a commonly used region growing technique (Gonzalez & Woods, 2002), here, region growing is performed by moving the boundary points radially away from the seed point iteratively. In this process, the centroid and boundary of each focal region are considered as the seed point and initial boundary, respectively.

Let for the nth focal region, $V_{n,0}$ be the set of B number of vertices of the mass at the initial stage i.e. $V_{n,0}$ is selected from the initial boundary after sampling it with equal angular distance from the centroid $c_c(xc, yc)$.

$$V_{n,0} = \left\{ v_i^n = (x_0(i), y_0(i)) | i = 1, 2, \cdots, B \right\},$$
$$xc = \frac{\sum_{i=1}^{B} x_0(i)}{B}, yc = \frac{\sum_{i=1}^{B} y_0(i)}{B}. \tag{2}$$

At tth iteration, the set of boundary pixels $V_{n,t}$ is obtained by forwarding the boundary pixels radially away from the centroid if they satisfy the following conditions:

- $Gr[(x_t(i), y_t(i))] \geq Gr[(x_{t-1}(i), y_{t-1}(i))]$, where $Gr[(x, y)]$ denotes the gradient at the point (x, y) along the direction of the straight line, connecting the point (x, y) and the seed point.
- The region growing will continue un-till $\frac{\text{mean}(\mathbf{I}(A_t^n))}{\text{mean}(\mathbf{I}(\lambda^n))} \leq \alpha$, where $0 < \alpha < 1$ is empirically selected; A_t^n and λ^n are the area of obtained mass region at tth iteration and the initial focal region, respectively for the n^{th} focal region.

A high dispersion may observe between the distances of vertices from centroid. To avoid this, boundary points are approximated using modal band analysis. In this step, vertices are divided

by a set of concentric equidistance (Δr) circular bands, centered at the seed point, as given by

$$B = \left\{ b_i | \Delta r \times (i-1) < b_i \leq \Delta r \times i \right\}_{i=1,2,\cdots,C},$$

where C is the total number of bands. Let the total number of vertices in b_i band be VB_i. Then the mth modal band is selected as dominant band if it contains the maximum number of vertices as given by $m = \arg\left\{ \max_i \left\{ VB_i \right\} \right\}$. Finally, the vertices located outside the dominant band are moved backward on the outer boundary of circle of the dominant band while vertices located inside of the inner boundary are moved forwarded on the inner boundary as following,

$$\hat{v} = \begin{cases} \Delta r \times m & \text{if } ||v - c_c||_2 \geq \Delta r \times m \\ \Delta r \times (m-1) & \text{if } ||v - c_c||_2 < \Delta r \times (m-1), \end{cases} \quad (3)$$

where $||\bullet||_2$ is the l_2 norm; $\hat{v}$ is the modified location of a vertex v;

4.1.4. Elementary false positive reduction

After the initial detection, unnecessary regions which are normal or may be a part of the same mass associated with another suspicious region, are removed from further processing by using contrast and distance criteria (Chakraborty et al., 2013).

4.1.5. Extraction of finer boundary

The coarse boundary obtained at the earlier step may not be able to represent the exact mass region. However, to classify them further precise segmentation is important. The Chen–Vess level set algorithm (Chan & Vese, 2001) is applied for this purpose on each ROI after cropping a square region enclosing the coarse boundary, which is used as the initial contour. The velocity of the movement is selected as $\Delta t = 0.1$ and the iterative process is continued until either the area of segmented region changes less than five pixels or maximum iteration (500) is reached. The parameter values are selected experimentally.

4.1.6. FP reduction with classifier

To remove FPs further we extract popularly used GLCM-based 14 haralick's features (Haralick, 1979; Haralick, Shanmugam, & Dinstein, 1973) from each ROI. GLCM descibes the spatial distribution of pixels in a neighborhood via computing the probability of occurrences of each pixel pair located at a specified distance and angle. To derive rotation invariant features, four matrices are calculated with angles {0°, 45°, 90°, and 135°} with empirically selected distance of one pixel and quantization levels of 128 and averaged to form a single resultant matrix. A naive Bayes classifier is then applied with these features for the classification of ROIs into normal and mass cases.

4.2. Classification of masses as benign or malignant

With the observation that in presence of mass the orientation of breast tissues changes from the normal, which may be different for benign and malignant, we investigate the angular distribution of tissue patterns of mammogram at different resolutions for mass classification and combine them with intensity-based texture information.

4.2.1. ROI selection

Based on the characteristics of benign and malignant masses, three different regions were defined for the analysis:

1. The entire mass region (M_1),
2. A region with width R outside the mass region (M_2),
3. A region M_3 with width R towards the inner and outer direction from the mass boundary i.e. total width of M_3 is $2R$;

R was computed based on the lesion size as

$$R = r_b * \frac{A_m}{A_b}.$$

where A_m is the area of a mass, r_b and A_b represent the radius and area of the bounding circle, respectively. The rubber band straightening transform has been employed on M_2 and M_3 to transform them into cartesian coordinate before applying feature extraction technique as the directional features perform better in the cartesian plane (Sahiner et al., 1998).

4.2.2. Multi-resolution decomposition into different scales and frequency

Wavelet decomposition is a popular method to analyze a signal at different resolution via decomposing the signal at different frequencies and scales (Mallat, 1998). Due to its similar working principles as that of human visual system, it has been effectively used in various image processing and computer vision applications such as image compression, enhancement, denoising, feature extraction etc. Since multi-resolution analysis of texture using wavelet has been successfully reported (Soulard & Carr, 2011), wavelet transform is used in this study.

The 2-D discrete wavelet transform (DWT), applied on the ROIs, is given by

$$W_\phi(k_1,k_2,k_3) = \frac{1}{\sqrt[2]{XY}} \sum_{x=1}^{X} \sum_{y=1}^{Y} \mathbf{I}(x,y) \phi_{k_1,k_2,k_3}(x,y),$$

$$W_\psi^i(k_0,k_2,k_3) = \frac{1}{\sqrt[2]{XY}} \sum_{x=1}^{X} \sum_{y=1}^{Y} \mathbf{I}(x,y) \psi^i_{k_0,k_2,k_3}(x,y), \quad (4)$$

where $X \times Y$ is the dimension of the input image; $\mathbf{I}(x, y)$ is intensity of the pixel located at (x, y) position of the image; ϕ and ψ are the scale and translation function, respectively; direction index is represented by $i = \{H, V, D\}$. Among the commonly used wavelets, such as Haar, Daubechies, Mexican hat etc., Haar wavelet has been selected in the present study for being simple and computationally efficient.

At each level of wavelet decomposition, the image is decomposed into four sub-bands— smoothed image (LL), vertical edges (LH), horizontal edges (HL), and diagonal edges (HH) of the original image. The smooth version of the image (LL) at a particular level is considered as the input of the next level. In this study, three levels of decomposition is considered. Fig. 3 shows the three level decompositions of the benign and malignant masses, shown in Fig. 1.

4.2.3. Extraction of statistical features from angular and intensity distribution of breast tissues

To measure the angular distribution of the parenchymal tissues, ACM-based statistical features are extracted from each level of decomposition of each ROI (i.e. M_1, M_2, and M_3). ACM was initially developed by Chakraborty et al. to characterize the angular distribution of orientated tissue patterns via quantifying the joint occurrence of oriented patterns angles, in context of architectural distortion detection (Chakraborty, Rangayyan, Banik, Mukhopadhyay, & Desautels, 2012a; 2012b). Two ACMs, defined using the angle information of tissues, are given below

$$ACM1_{(d,\theta)}(\varphi_1,\varphi_2) = \frac{P_c(\varphi_1,\varphi_2)}{\sum_{\varphi_1=1}^{N_\theta} \sum_{\varphi_2=1}^{N_\theta} P_c(\varphi_1,\varphi_2)},$$

$$ACM2_{(d,\theta)}(\varphi_1,\varphi_2) = \frac{P_m(\varphi_1,\varphi_2)}{\sum_{\varphi_1=1}^{N_\theta} \sum_{\varphi_2=1}^{N_\theta} P_m(\varphi_1,\varphi_2)}, \quad (5)$$

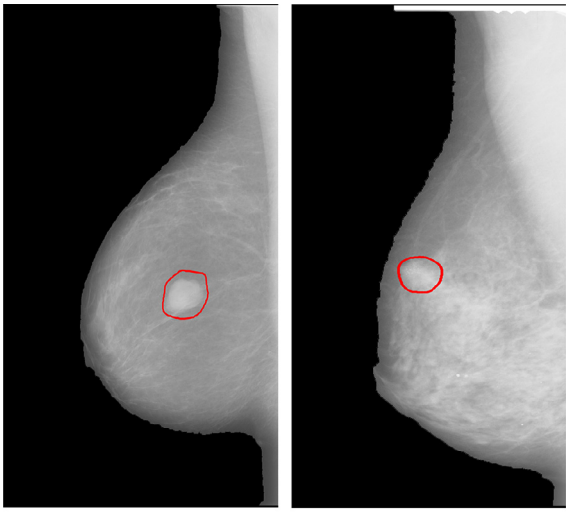

(a) (b)

Fig. 1. Two exemplar mammographic images containing (a) benign and (b) malignant masses.

where $ACM1_{(d,\theta)}(\varphi_1, \varphi_2)$ and $ACM2_{(d,\theta)}(\varphi_1, \varphi_2)$ represent the probability of occurrence of the pair of angles (φ_1, φ_2) separated at a distance and angle of d and θ, respectively; $P_c(\varphi_1, \varphi_2)$ and $P_m(\varphi_1, \varphi_2)$ are the total number of pixels and sum of the gradient magnitude of all pixel pairs with orientation from φ_1 to φ_2 and separation of (d, θ); N_θ is the number of levels after quantization.

ACMs are computed on each sub-band. Sobel operator of size 7×7 is used for obtaining the gradient information of each pixel. For each of the decomposed image, final rotation invariant ACMs are obtained by averaging four ACMs computed at four different angles ($\theta = 0°$, 45°, 90°, and 135°) with $d = 1$. N_θ is empirically selected as 64. Hence, for each region M_1, M_2, and M_3 24 $(4 \times 3 \times 2)$ ACMs (ACM1 and ACM2) are computed for the extraction of statistical features. Haralick's 14 statistical features are then computed from each of the ACMs to classify the mass. The ACMs derived from the three decomposed levels for the benign and malignant masses, shown in Fig. 1, are provided in Figs. 4 and 5. For the benign mass ACMs are sparser than malignant mass which indicate the wider and random spread of oriented patterns in the malignant mass than benign one. The figures also indicate that although vertical component of 1st level decomposition of both masses have similar ACM patterns, the same from the 2nd level is different between them. Similar to other texture analysis, this demonstrates the importance of different resolutions; each can capture different discriminatory characteristics. Since Haralick's features from GLCM were widely used for mass classification, we also compute GLCM-based Haralick's features from each level of decomposition of each ROI. Distance and quantization levels, for calculating GLCM, are considered as one and 128, respectively. The two main purpose of extracting GLCM-based features are to compare and combine them with the proposed features for the classification of masses. By combination we utilize both intensity and directional edge information of masses for their classification. The GLCM matrices for the three levels of the benign and malignant masses, displayed in Fig. 1, are shown in Fig. 6.

A total of 1512 $(14 \times 4 \times 3 \times 3 \times 3)$ features have been computed from all regions.

4.2.4. Feature selection and classification

To select the discriminatory features, so as to reduce the computational complexity and to achieve more accurate classification performance stepwise logistic regression method (Ramsey & Schafer, 1997) is used in this study. Finally, naive Bayes classifier and Random Forest (RF) techniques have been employed for the classification of masses using the selected features. For RF, 5000 trees are considered with the minimum number of observations per tree as one and number of variables per random splitting as square root of the variables, respectively. In Naïve-bayes classifier

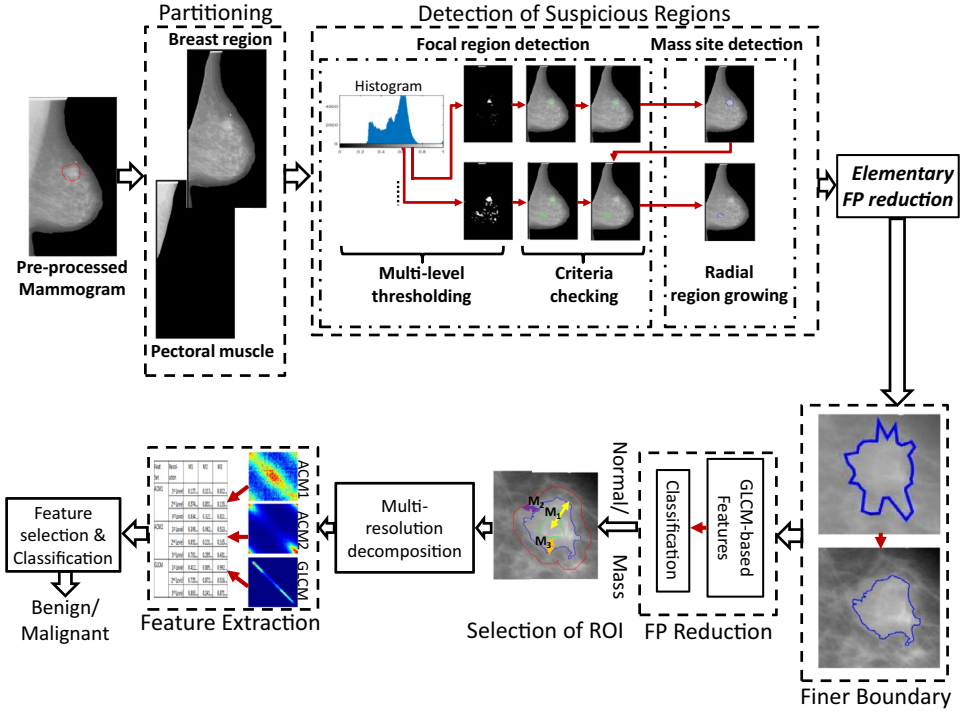

Fig. 2. Block diagram of the proposed system for mass detection and classification.

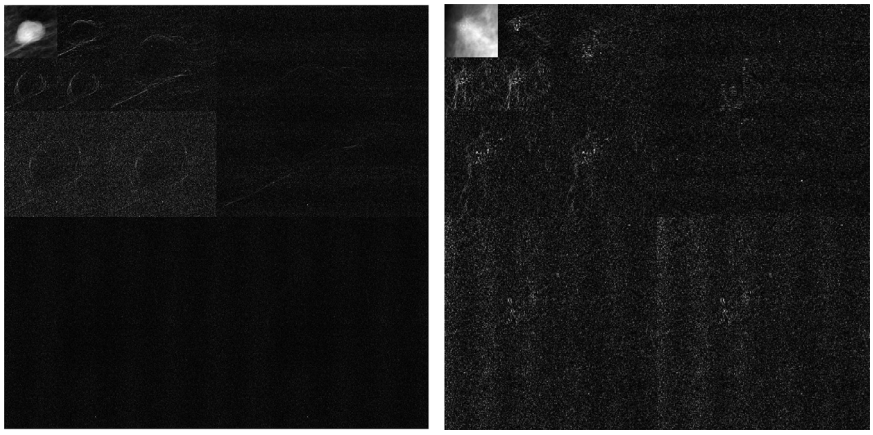

Fig. 3. Three level decompositions for the benign and malignant masses shown in Fig. 1.

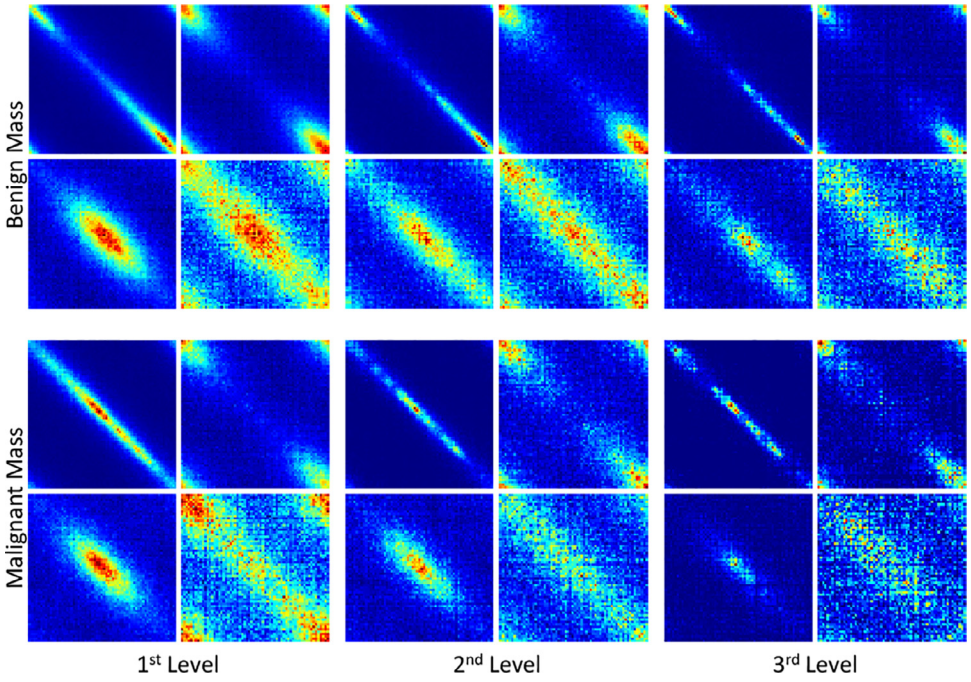

Fig. 4. ACM1 computed from the four subbands (LL, HL, LH, and HH) of different resolutions of M1. The top row is for benign mass and the bottom row is for malignant mass. For better visualization ACMs are represented with pseudo color.

prior probability is computed from the training data and Gaussian function is used as the likelihood function.

4.2.5. Evaluation of two stage classification

To avoid overfitting the performance of the proposed two stage classification, i.e., classification of ROIs into mass or normal and into benign or malignant is evaluated with 10-fold cross validation technique. In the second stage, since some of the non-mass regions may be selected a masses, we distinguish malignant masses from the others. Moreover, the average of 10 runs is considered as the final evaluation metric with feature selection within each training fold. In addition, for avoiding bias all the ROIs for a single patient are either kept in training or test set.

5. Results and discussion

The proposed mass detection and classification schemes are implemented using Matlab, version R2015a (Natick, MA, USA), on a computer with an Intel i3 processor having frequency 2.27 GHz, 4GB RAM, and Windows 7 operating system. The current section is divided into two subsections. The performance of the proposed mass detection scheme using multi-level thresholding followed by radial region growing and mass classification scheme using multi-resolution features is analyzed in details in Sections 5.1 and 5.2, respectively.

5.1. Performance of the mass detection scheme

The optimum values of the parameters, such as step size (δ), diameter of the disk-shaped element (Γ), tolerance in the region growing algorithm (α), width of the concentric bands (b) have been selected by examining their effects on mass detection as illustrated in Table 1. After the initial detection algorithm i.e. after elementary FPs reduction, a total of 5327 ROIs, including 799 TP and 4528 FPs are obtained which corresponds to a sensitivity of 89.8% at 3.6 FP/image. The detection rate for benign masses is lower than that for malignant masses. The method fails to detect 39 malignant and 52 benign masses which provides a sensitivity of 91.1% and 88.4%, respectively for malignant and benign mass detection. Application of GLCM-based haralick's features with naive-bayes classifier achieves an A_z of 0.77 and sensitivities of 85% at 1.4 FP/image for FP reduction. Some of the detected cases are shown

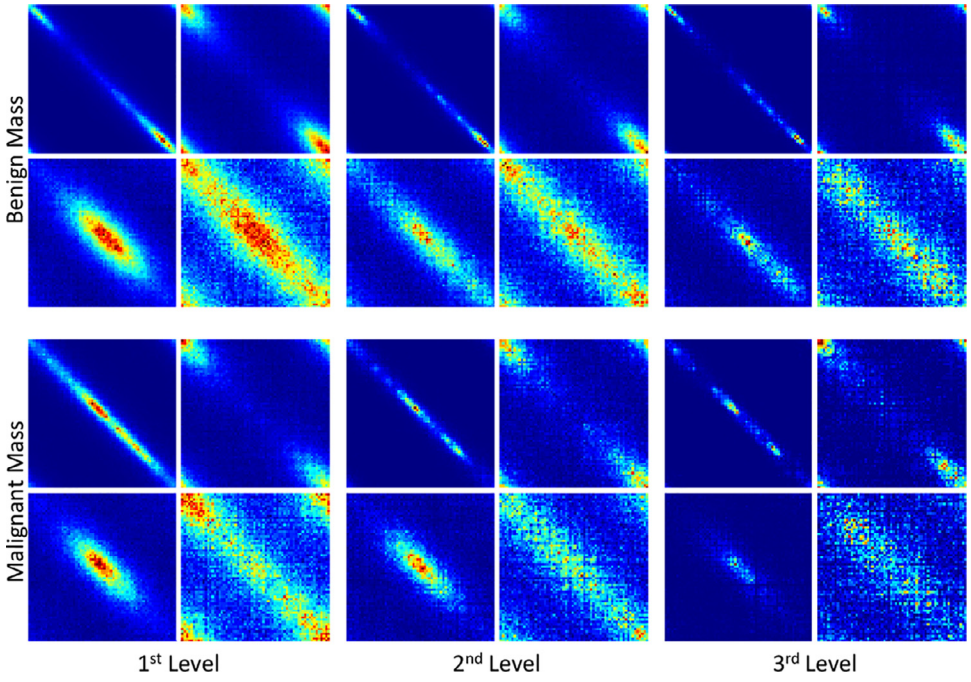

Fig. 5. ACM2 computed from the four subbands (LL, HL, LH, and HH) of different resolutions of M1. The top row is for benign mass and the bottom row is for malignant mass. For better visualization ACMs are represented with pseudo color.

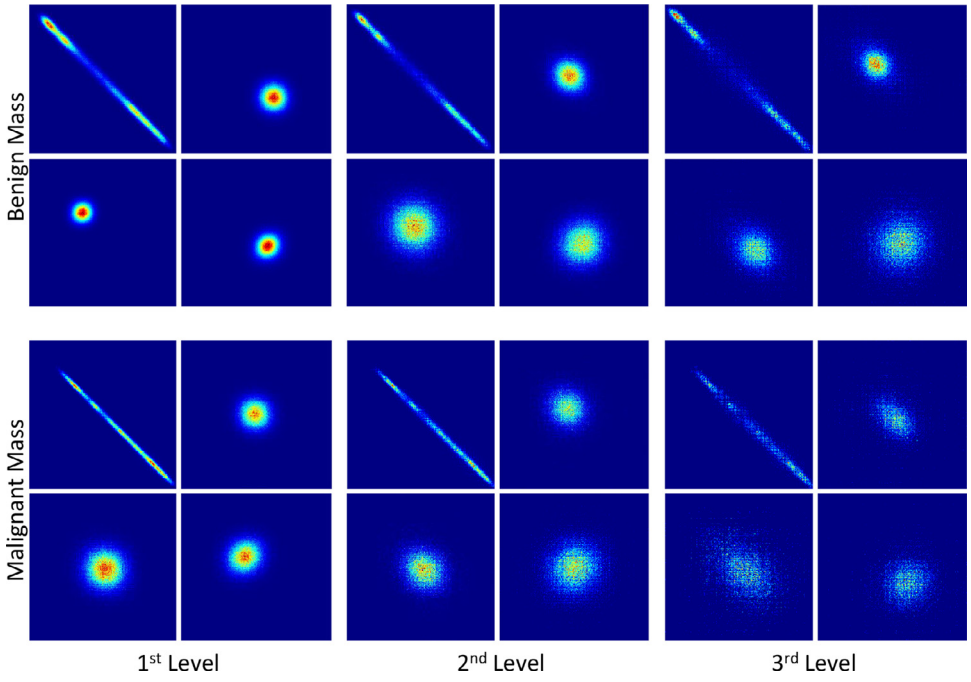

Fig. 6. GLCM computed from the four subbands (LL, HL, LH, and HH) of different resolutions of M1. The top row is for benign mass and the bottom row is for malignant mass. For better visualization ACMs are represented with pseudo color.

in Fig. 7, among which last four masses are occluded in dense tissue. This demonstrates the efficacy of our method in detecting occluded masses.

5.2. Performance of mass classification scheme

In this section, classification efficacy of the multi-resolution features discussed in Section 4.2 is validated only on the cases that has been successfully detected as mass region.

The performance is evaluated in terms of the A_z and classification accuracy (A_{cc}). The average A_z and A_{cc} over 10 runs are considered as the evaluation metrics in discriminating the masses. All three types of features (GLCM, ACM1, and ACM2-based) from each of the M_1, M_2, and M_3 regions are analyzed with naive Bayes and RF classifiers and the results are summarized in Tables 2 and 3, respectively.

It is observed from Tables 2 and 3 that the proposed multi-resolution features carry discriminative information between benign/normal and malignant masses. The best A_z value of

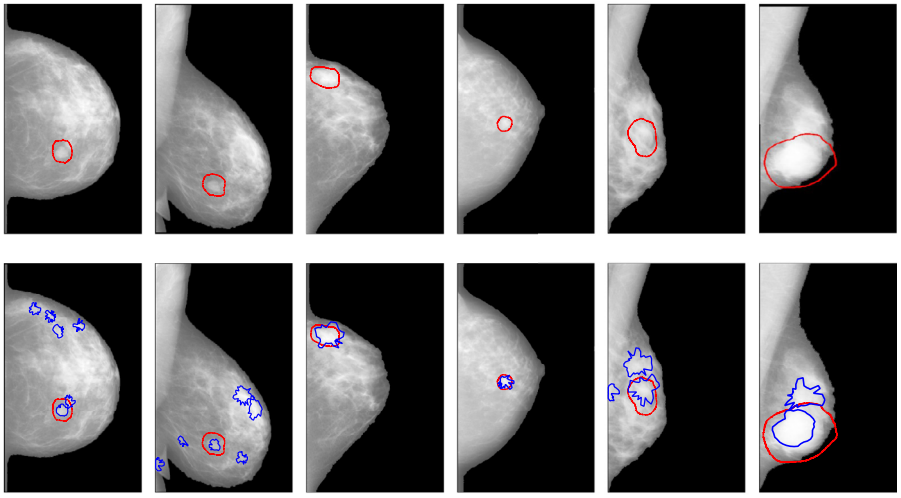

Fig. 7. Top row: original mammograms, containing masses, from the DDSM database after the preprocessing step. The corresponding detection results are shown with blue contour in the bottom row. The true mass regions are marked by red circles.

Table 1
Experimentally selected values of the different parameters used in the proposed procedure.

Name of parameter	Trial values	Optimal value
Step size (δ)	0.01, 0.03, 0.05, 0.07, 0.09	0.05
Diameter of the disk-shaped element (Γ)	1.2, 2, 2.8, 4.0, 4.8 (mm)	2.8 (mm)
Tolerance in the region growing algorithm (α)	0.6, 0.7, 0.8, 0.85, 0.9, 0.95, 0.97, 0.99	0.85
Width of the concentric bands (b)	2, 4, 6, 8, 10, 12 (mm)	8 (mm)

0.89 ± 0.003, 0.87 ± 0.001, and 0.88 ± 0.003 is obtained with ACM1, ACM2, and GLCM features from M_3 regions using RF classifier. In general ACM-based features (ACM1) show better performance than GLCM-based features, especially for M_1. The combination of all feature sets within each region improves the performance than individual groups. The GLCM features provide the intensity distribution of a region, whereas ACM1 and ACM2 features quantify the angular distribution of oriented patterns. Consequently, when GLCM features are fused with ACM1 and ACM2, the combined features are able to capture both intensity and edge information, resulting better discrimination between benign and malignant masses.

The performance of feature sets from each region clearly indicates that textures from all three regions (M_1, M_2, and M_3) carry significant discriminating information. Hence, we investigate their combined effect. Significant improvement is not observed when each features set from all regions are combined and analyzed with RF (except for ACM2). For example, both GLCM-based features from M_3 and from all regions (M_1, M_2, and M_3) provide an A_z value of 0.88. However, classification with naive Bayes provides better performance for combination compared to individual region. The concatenation of all features from all regions show significant performance with an A_z value of 0.92 ± 0.001 with an A_{cc} of 83.30 ± 0.35 using RF. Similarly, naive Bayes classifier delivers an A_z value of 0.84 ± 0.001 with an A_{cc} of 79.26 ± 0.27. The ROC curves for different features extracted from different regions are provided in Fig. 8. When features from different regions are combined it is observed that more features are selected from M_3 region, which indicates the better discriminatory power of the region surrounding mass boundary.

The performance of the proposed features is better with random forest than naive Bayes classifier. However, it should also be noted that in naive Bayes classifier no parameter tuning is required, whereas the selection of parameters is important for RF as the performance is sensitive to the proper selection of parameters.

We also analyzed the effect of resolution at which features are extracted with a random forest classifier and the results are provided in Table 4. It is observed that the combinations of features from all regions extracted at the first and second level decomposition provides better performance compared to features extracted without wavelet decomposition. However, further decomposition beyond second level does not improve the performance. The combination of features from first and second level provides better performance than their individuals. The performance is marginally improved compared to increasing computational complexity when features of third level decomposition are fused with earlier combination. Hence, we restricted our study till third level decomposition.

5.3. Comparison with other methods

Only a few studies focussed on mass detection followed by classification (Casti et al., 2016; Mudigonda et al., 2001; Polakowski

Table 2
The mean area under the ROC curve (A_z) and mean accuracy (A_{cc}) obtained with different feature sets using naive Bayes classifier and 10-fold cross-validation. The results are provided in the form of $\mu \pm \sigma$, where μ = mean and σ = standard deviation.

Feature	M_1		M_2		M_3		All Regions	
Set	A_z	A_{cc}	A_z	A_{cc}	A_z	A_{cc}	A_z	A_{cc}
GLCM	0.71 ± 0.002	65.47 ± 0.44	0.76 ± 0.001	69.81 ± 0.19	0.80 ± 0.001	73.03 ± 0.26	0.82 ± 0.001	76.43 ± 0.46
*ACM*1	0.69 ± 0.003	63.95 ± 0.41	0.76 ± 0.0004	69.26 ± 0.15	0.77 ± 0.001	71.21 ± 0.28	0.83 ± 0.001	77.84 ± 0.14
*ACM*2	0.76 ± 0.001	71.69 ± 0.15	0.75 ± 0.001	69.13 ± 0.001	0.70 ± 0.001	66.71 ± 0.29	0.78 ± 0.001	69.72 ± 0.15
All Features	0.79 ± 0.001	70.81 ± 0.003	0.76 ± 0.0004	69.12 ± 0.19	0.77 ± 0.001	71.01 ± 0.17	0.84 ± 0.001	79.26 ± 0.27

Table 3
The mean area under the ROC curve (A_z) and mean accuracy (A_{cc}) obtained with different feature sets using RF and 10-fold cross-validation. The results are provided in the form of $\mu \pm \sigma$, where μ =mean and σ =standard deviation.

Feature	M_1		M_2		M_3		All Regions	
Set	A_z	A_{cc}	A_z	A_{cc}	A_z	A_{cc}	A_z	A_{cc}
GLCM	0.79 ± 0.003	71.67 ± 0.62	0.87 ± 0.003	78.84 ± 0.29	0.88 ± 0.003	79.94 ± 0.37	0.88 ± 0.002	81.88 ± 0.17
*ACM*1	0.84 ± 0.002	76.03 ± 0.42	0.88 ± 0.001	78.64 ± 0.51	0.89 ± 0.003	78.79 ± 0.66	0.89 ± 0.001	82.0 ± 0.0014
*ACM*2	0.86 ± 0.004	77.52 ± 0.38	0.87 ± 0.001	78.88 ± 0.42	0.87 ± 0.001	78.98 ± 0.33	0.90 ± 0.001	81.99 ± 0.44
All Features	0.89 ± 0.002	80.74 ± 0.11	0.89 ± 0.001	80.20 ± 0.50	0.90 ± 0.003	81.54 ± 0.43	0.92 ± 0.001	83.30 ± 0.35

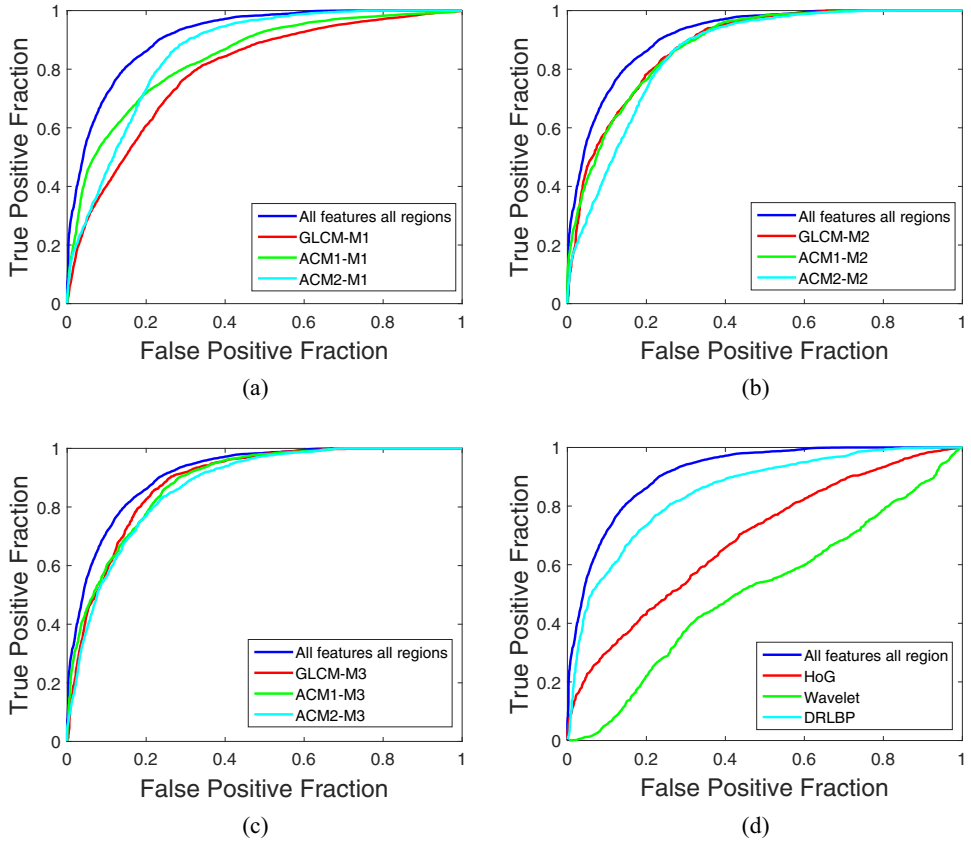

Fig. 8. ROC curves obtained using RF classifier for different feature set extracted from (a) M1 (b) M2 and (c) M3 region, respectively. (d) Comparative ROC curves for the proposed method and existing feature sets.

Table 4
The performance of features extracted at different resolution and using RF classifier. The results are provided in the form of $\mu \pm \sigma$, where μ =mean and σ =standard deviation.

Resolution Level (ϕ)	A_z	A_{cc} (%)
Without decomposition	0.81 ± 0.005	72.01 ± 0.46
1st level	0.87 ± 0.004	80.06 ± 0.12
2nd level	0.87 ± 0.002	81.20 ± 0.36
3rd level	0.86 ± 0.001	81.39 ± 0.45
$(1 \cup 2)$nd level	0.92 ± 0.001	82.42 ± 0.41
$(1 \cup 2 \cup 3)$rd level	0.92 ± 0.001	83.30 ± 0.35

et al., 1997). Although it is unfair to compare the proposed method with these techniques, directly, due to the use of different datasets and unavailability of several parameters (Casti et al., 2016), we perform a comparative analysis with their reported results. Polakowski et al. (1997) obtained 100% detection accuracy with a FP rate of 1.8/image for segmenting and a sensitivity of 92% for locating malignant masses with a private dataset of 272 images, containing 36 malignant and 53 benign masses. Although the method reported in (Polakowski et al., 1997) delivers higher performance than the proposed method, the dataset was limited for that study. As discussed in the introduction, Mudigonda et al. (Mudigonda et al., 2001) achieved a sensitivity of 81% at 2.2 FPs/image for mass detection and an A_z value of 0.79 for classification with a dataset of 56 images containing 30 benign, 13 malignant, and 13 normal cases from the mini-MIAS database. Casti et al. obtained a sensitivity of 0.80 at 5.21 FPs/image for the detection and an A_z value of 0.61 for the diagnosis with a dataset of 785 normal and 877 masses, containing 416 malignant cases from the DDSM. In comparison, the proposed method achieved a sensitivity of 85.0% at 1.4FP/image for the detection of masses and an A_z value of 0.92 for the classification with a large number of images from the DDSM. This demonstrates the efficacy of the proposed method over the recent state-of-the-art techniques.

Moreover, we made a direct comparison of our proposed mass detection and diagnosis algorithms with some of the recently proposed methods inTables 5–7. Table 5 establishes the efficacy of the detection algorithms over the existing approaches. It is to be noted that although Martins et al. obtained slightly better performance than the proposed method, we experimented with a large set of images.

Table 5
Comparison of performance among different mass detection schemes in terms of sensitivity and FPs/image.

Methods	Database	No of Images		Sensitivity	FPs/ image
		Mass	Normal	(in %)	
Dominguez and Nandi (2008)	mini-MIAS	All	–	80.0	2.3
Kozegar, Soryani, Minaei, and Domingues (2013)	mini-MIAS	All	–	90.0	4.5
Campanini, Dongiovanni, Iampieri, Lanconelli, Masotti, and Palermo (2004)	DDSM	1112	800	80.0	1.1
Martins, Junior, Silva, de Paiva, and Gattass (2009)	DDSM	260	173	86.0	1.2
Liu and Feng (2011)	DDSM	231	–	76.8	1.36
Tai et al. (2014)	DDSM	258	50	90.0	2.6
Dhungel, Carneiro, and Bradley (2015)	DDSM-BCRP	316	–	75.0	4.8
Min, Chandra, Dhungel, Crozier, and Bradley (2017)	DDSM-BCRP	163	–	77.0	3.93
Proposed method	DDSM	847	410	80.0	1.0
				90.0	1.4

Table 6
Comparison of performance among different mass diagnosis schemes in terms of A_z and A_{cc}.

Methods	Database	No of ROIs		A_z	A_{cc}%
		Benign	Malignant		(%)
Dhungel, Carneiro, and Bradley (2017)	INbreast	410		0.8	–
Tsochatzidis et al. (2017)	DDSM	400		0.85	81.0
Akselrod-Ballin, Karlinsky, Alpert, Hashoul, Ben-Ari, and Barkan (2017)	DDSM	850		–	78.0
Al-Masni, Al-Antari, Park, Gi, Kim, and Rivera (2017)	DDSM	300	300	0.88	85.52
Antropovaa, Huynh, and Giger (2017)	FFDM	328	411	0.86	–
Rouhi, Jafari, Kasaei, and Keshavarzian (2015)	DDSM	74	96	0.95	95.01
Proposed method	DDSM	371	386	0.87	77.89

Table 7
Comparison of the proposed features with others for the benign and malignant mass classification.

Features	naive Bayes		RF	
	A_z	A_{cc}	A_z	A_{cc}
DWT	0.613	59.45	0.621	60.12
HOG	0.658	62.19	0.668	62.46
DRLBP	0.731	68.80	0.830	74.75
Proposed method	0.785	72.79	0.866	77.89

Earlier we provided the performance of the proposed features in classification of benign/normal and malignant in Tables 2 and 3. However, we included only the detected benign and malignant masses for comparison as the competing schemes considered only these two types of cases and the results are provided in Table 6. Additionally, we have implemented some of the existing features–DWT (Mallat, 1998), histograms of gradients (HoG) (Buciu & Gacsadi, 2011), discriminative robust LBP (DRLBP) (Rabidas, Midya, Sadhu, & Chakraborty, 2016) and tested them on the same dataset used here. The features are compared in terms of A_z value (Table 7). Since combination of all features from all regions provides the best performance we selected this set for the comparison purpose. An AUC of 0.87 and an accuracy of 77.89 are achieved with the features using random forest classifier (Table 7). The obtained ROC curves are also provided in Fig. 8. It is evident that the proposed scheme outperforms the competing methods.

6. Conclusions

An automatic system for both detection and classification of masses can help to treat patients efficiently. The proposed method can detect masses effectively. Multi-resolution features, characterizing oriented tissue structures, show discriminating power for benign and malignant mass classification. The combination of ACMs with GLCM provides better performance than individuals via capturing both intensity and directional edge information. Though different regions associated to mass has potential to separate masses, the boundary surrounded region which captures both inside and outside information carries the best. Further work is in progress to reduce FPs using improved radiographic and quantitative features or a three class deep learning approach for the classification of normal, benign, and malignant masses.

References

Akselrod-Ballin, A., Karlinsky, L., Alpert, S., Hashoul, S., Ben-Ari, R., & Barkan, E. (2017). A cnn based method for automatic mass detection and classification in mammograms. *Computer Methods in Biomechanics and Biomedical Engineering: Imaging & Visualization*, 1–8.

Al-Masni, M. A., Al-Antari, M. A., Park, J. M., Gi, G., Kim, T. Y., Rivera, P., et al. (2017). Detection and classification of the breast abnormalities in digital mammograms via regional convolutional neural network. In *39th annual international conference of the IEEE engineering in medicine and biology society (EMBC)* (pp. 113–117).

American Cancer Society (2015). *Global cancer facts and figures* (3rd ed.). Atlanta, GA: American Cancer Society.

Antropovaa, N., Huynh, B. Q., & Giger, M. L. (2017). A deep feature fusion methodology for breast cancer diagnosis demonstrated on three imaging modality datasets. *Medical Physics, 44*(10), 5162–5171.

Buciu, I., & Gacsadi, A. (2011). Directional features for automatic tumor classification of mammogram images. *Biomedical Signal Processing and Control, 6*(4), 370–378.

Campanini, R., Dongiovanni, D., Iampieri, E., Lanconelli, N., Masotti, M., Palermo, G., et al. (2004). A novel featureless approach to mass detection in digital mammograms based on support vector machines. *Physics in Medicine and Biology, 49*, 961–975.

Casti, P., Mencattini, A., Salmeri, M., Ancona, A., Mangeri, F., Pepe, M., et al. (2016). Contour-independent detection and classification of mammographic lesions. *Biomedical Signal Processing and Control, 25*, 165–177.

Casti, P., Mencattini, A., Salmeri, M., Ancona, A., Mangieri, F., & Rangayyan, R. M. (2014). Development and validation of a fully automated system for detection and diagnosis of mammographic lesions. In *36th annual international conference of the IEEE engineering in medicine and biology society* (pp. 4667–4670).

Chakraborty, J., Midya, A., Mukhopadhyay, S., & Sadhu, A. (2013). Automatic characterization of masses in mammograms. In *6th international conference on biomedical engineering and informatics (BMEI), Berlin, Germany* (pp. 111–115).

Chakraborty, J., Mukhopadhyay, S., Singla, V., Khandelwal, N., & Bhattacharyya, P. (2011). Automatic detection of pectoral muscle using average gradient and shape based feature. *Journal of Digital Imaging, 25*(3), 387–399.

Chakraborty, J., Mukhopadhyay, S., Singla, V., Khandelwal, N., & Rangayyan, R. M. (2012). Detection of masses in mammograms using region growing controlled by multilevel thresholding. In *25th IEEE international symposium on computer-based medical system (CBMS), Rome, Italy* (pp. 1–6).

Chakraborty, J., Mukhopadhyay, S., Singla, V., Khandelwal, N., & Rangayyan, R. M. (2013). Hybrid region growing controlled by multilevel thresholding for the detection of masses in mammograms. *Medical Image Analysis*.

Chakraborty, J., Rangayyan, R. M., Banik, S., Mukhopadhyay, S., & Desautels, J. E. L. (2012a). Detection of architectural distortion in prior mammograms using statistical measures of orientation of texture. In *Proceedings of spie medical imaging 2012: Computer aided diagnosis, San Diego, CA: 8315*.

Chakraborty, J., Rangayyan, R. M., Banik, S., Mukhopadhyay, S., & Desautels, J. E. L. (2012b). Statistical measures of orientation of texture for the detection of architectural distortion in prior mammograms of interval cancer. *Journal of Electronic Imaging, 21(3)*(Article number 033010), 1–13.

Chan, T. F., & Vese, L. A. (2001). Active contours without edges. *IEEE Transactions on Image Processing, 10*(2), 266–277.

Cheng, H. D., Shi, X. J., Min, R., Hu, L. M., Cai, X. P., & Du, H. N. (2006). Approaches for automated detection and classification of masses in mammograms. *Pattern Recognition, 39*, 646–668.

Choi, J. Y., Kim, D. H., & Ro, Y. M. (2012). Combining multiresolution local binary pattern texture analysis and variable selection strategy applied to computer-aided detection of breast masses on mammograms. In *IEEE-embs international conference on biomedical and health informatics (bhi), 2012* (pp. 495–498).

Dhungel, N., Carneiro, G., & Bradley, A. P. (2015). Automated mass detection in mammograms using cascaded deep learning and random forests. In *International conference on digital image computing: Techniques and applications (dicta-2015)* (pp. 1–8).

Dhungel, N., Carneiro, G., & Bradley, A. P. (2017). Fully automated classification of mammograms using deep residual neural networks. In *IEEE 14th international symposium on biomedical imaging (ISBI 2017)* (pp. 310–314).

Dominguez, A. R., & Nandi, A. K. (2008). Detection of masses in mammograms via statistically based enhancement multilevel-thresholding segmentation, and region selection. *Computerized Medical Imaging and Graphics, 32*(4), 304–315.

Eltonsy, N. H., Tourassi, G. D., & Elmaghraby, A. S. (2007). A concentric morphology model for the detection of masses in mammography. *IEEE Transactions on Medical Imaging, 26*(06), 880–889.

Eltoukhy, M. M., Faye, I., & Samir, B. B. (2012). A statistical based feature extraction method for breast cancer diagnosis in digital mammogram using multiresolution representation. *Computers in Biology and Medicine*, 123–128.

Ferlay, J., Shin, H. R., Bray, F., Forman, D., Mathers, C., & Parkin, D. M. (2010). Globocan 2008 v2.0, cancer incidence and mortality worldwide: IARC CancerBase no. 10 [internet]. Available at http://globocan.iarc.fr, accessed on 5 December, 2012.

Ferlay, J., Soerjomataram, I., Ervik, M., Dikshit, R., Eser, S., Mathers, C., et al. (2013). Globocan 2012 v1.0, cancer incidence and mortality worldwide: IARC CancerBase no. 11 [internet]. Available at http://globocan.iarc.fr, accessed on 23 July, 2017.

Ferrari, R. J., Rangayyan, R. M., Borges, R. A., & Frère, A. F. (2004). Segmentation of the fibro-glandular disc in mammograms using Gaussian mixture modeling. *Medical and Biological Engineering and Computing, 42*, 378–387.

Gao, X., Wang, Y., Li. , X., & Tao, D. (2010). On combining morphological component analysis and concentric morphology model for mammographic mass detection. *IEEE Transactions on Medical Imaging, 14*(2), 266–273.

Gonzalez, R., & Woods, R. (2002). *Digital image processing* (2nd). Upper Saddle River, NJ: Prentice-Hall.

Gorgel, P., Sertbas, A., Kilic, N., Ucan, O. N., & Osman, O. (2009). Mammographic mass classification using wavelet based support vector machine. *Journal of Electrical & Electronics Engineering, 9*(1).

Haralick, R. M. (1979). Statistical and structural approaches to texture. *Proceedings of the IEEE, 67*, 786–804.

Haralick, R. M., Shanmugam, K., & Dinstein, I. (1973). Textural features for image classification. *IEEE Transactions on Systems, Man, Cybernetics, 3*(6), 610–622.

Heath, M., Bowyer, K., Kopans, D., Moore, R., & Kegelmeyer, W. P. (2001). The digital database for screening mammography. In *Proceedings of the fifth international workshop on digital mammography* (pp. 212–218). Medical Physics Publishing.

Islam, M. J., Ahmadi, M., & Sid-Ahmed, M. A. (2010). Computer-aided detection and classification of masses in digitized mammograms using artificial neural network. In Y. Tan, Y. Shi, & K. Tan (Eds.), *Advances in swarm intelligence*. In *Lecture Notes in Computer Science: 6146* (pp. 327–334). Springer Berlin Heidelberg.

Junior, G. B., da Rocha, S. V., Gattass, M., Silva, A. C., & de Paiva, A. C. (2013). A mass classification using spatial diversity approaches in mammography images for false positive reduction. *Expert Systems with Applications, 40*(18), 7534–7543.

Kobatake, H., Murakami, M., Takeo, H., & Nawano, S. (1999). Computerized detection of malignant tumors on digital mammograms. *IEEE Transactions on Medical Imaging, 18*(5), 369–378.

Kozegar, E., Soryani, M., Minaei, B., & Domingues, I. (2013). Assessment of a novel mass detection algorithm in mammograms. *Journal of Cancer Research and Therapeutics, 9*(4), 592–600.

Liu, X., & Feng, Z. (2011). A new automatic method for mass detection in mammography with false positives reduction by support vector machine. In *4th international conference on biomedical engineering and informatics (BMEI), Shanghai, China* (pp. 33–37).

Liu, X., & Zeng, Z. (2015). A new automatic mass detection method for breast cancer with false positive reduction. *Neurocomputing, 152*, 388–402.

Mahersia, H., Boulehmi, H., & Hamrouni, K. (2016). Development of intelligent systems based on Bayesian regularization network and neuro-fuzzy models for mass detection in mammograms: A comparative analysis. *Computer methods and programs in biomedicine, 126*, 46–62.

Mallat, S. G. (1998). *A wavelet tour of signal processing*. San Diego, CA: Academic Press.

Martins, L. O., Junior, G. B., Silva, A. C., de Paiva, A. C., & Gattass, M. (2009). Detection of masses in mammograms using K-means and support vector machine. *Electronic Letters on Computer Vision and Image Analysis, 8*(2), 39–50.

Mazurowski, M. A., Lo, J. Y., Harrawood, B. P., & Tourassi, G. D. (2009). CADx of mammographic masses and clustered microcalcifications: A review. *Medical Physics, 36*(6), 2052–2068.

Midya, A., & Chakraborty, J. (2015). Classification of benign and malignant masses in mammograms using multi-resolution analysis of oriented patterns. In *IEEE 12th international symposium on biomedical imaging (ISBI)* (pp. 411–414).

Min, H., Chandra, S. S., Dhungel, N., Crozier, S., & Bradley, A. P. (2017). Multi-scale mass segmentation for mammograms via cascaded random forests. In *IEEE 14th international symposium on biomedical imaging (ISBI-2017)* (pp. 113–117).

Mohanty, A. K., Senapati, M. R., Beberta, S., & Lenka, S. K. (2013). Texture-based features for classification of mammograms using decision tree. *Neural Computing and Applications, 23*(3), 1011–1017.

Mudigonda, N. R., Rangayyan, R. M., & Desautels, J. E. L. (2001). Detection of breast masses in mammograms by density slicing and texture flow-field analysis. *IEEE Transactions on Medical Imaging, 20*(12), 1215–1227.

Muramatsu, C., Hara, T., Endo, T., & Fujita, H. (2016). Breast mass classification on mammograms using radial local ternary patterns. *Computers in Biology and Medicine, 72*, 43–53.

Nascimento, M. Z., Martins, A. S., Neves, L. A., Ramos, R. P., Flores, E. L., & Carrijo, G. A. (2013). Classification of masses in mammographic image using wavelet domain features and polynomial classifier. *Expert Systems with Applications, 40*, 6213–6221.

Oliver, A., Freixenet, J., Mart, J., Prez, E., Pont, J., Denton, E. R. E., et al. (2010). A review of automatic mass detection and segmentation in mammographic images. *Medical Image Analysis, 14*, 87–110.

Pak, F., Kanan, H. R., & Alikhassi, A. (2015). Breast cancer detection and classification in digital mammography based on non-subsampled contourlet transform (nsct) and super resolution. *Computer Methods and Programs in Biomedicine, 122*(2), 89–107.

Petrick, N., Chan, H., Wei, D., Sahiner, B., Helvie, M., & Adler, D. (1996). Automated detection of breast masses on mammograms using adaptive contrast enhancement and texture classification. *Medical Physics, 23*(10), 1685–1696.

Petrick, N., Chan, H. P., & Sahiner, B. (1999). Combined adaptive enhancement and region-growing segmentation of breast masses on digitized mammograms. *Medical Physics, 26*(3), 1642–1654.

Polakowski, W. E., Cournoyer, D. A., Rogers, S. K., DeSimio, M. P., Ruck, D. W., Hoffmeister, J. W., et al. (1997). Computer-aided breast cancer detection and diagnosis of masses using difference of gaussian and derivative-based feature saliency. *IEEE Transactions on Medical Imaging, 16*(6), 811–819.

Rabidas, R., Chakraborty, J., & Midya, A. (2017). Analysis of 2D singularities for mammographic mass classification. *IET Computer Vision, 11*(1), 22–32.

Rabidas, R., Midya, A., & Chakraborty, J. (2017). Neighborhood structural similarity mapping for the classification of masses in mammograms. *IEEE Journal of Biomedical and Health Informatics*. doi: 10.1109/JBHI.2017.2715021 (in press).

Rabidas, R., Midya, A., Sadhu, A., & Chakraborty, J. (2016). Benign-malignant mass classification in mammogram using edge weighted local texture features. In *Proceedings of spie medical imaging 2016: Computer aided diagnosis, San Diego, CA: 9785*. 97851X–97851X6.

Ramos, R. P., do Nascimento, M. Z., & Pereira, D. C. (2012). Texture extraction: An evaluation of ridgelet, wavelet and co-occurrence based methods applied to mammograms. *Expert Systems with Applications, 39*(12), 11036–11047.

Ramsey, F. L., & Schafer, D. W. (1997). *The statistical sleuth: A course in methods of data analysis*. Belmont, CA: Duxbury Press.

Reyad, Y. A., Berbar, M. A., & Hussain, M. (2014). Comparison of statistical, LBP, and multi-resolution analysis features for breast mass classification. *Journal of Medical Systems, 38*(9), 1–15.

da Rocha, S. V., Junior, G. B., Silva, A. C., de Paiva, A. C., & Gattass, M. (2016). Texture analysis of masses malignant in mammograms images using a combined approach of diversity index and local binary patterns distribution. *Expert Systems with Applications, 66*, 7–19.

Rouhi, R., & Jafari, M. (2016). Classification of benign and malignant breast tumors based on hybrid level set segmentation. *Expert Systems with Applications, 46*, 45–59.

Rouhi, R., Jafari, M., Kasaei, S., & Keshavarzian, P. (2015). Benign and malignant breast tumors classification based on region growing and cnn segmentation. *Expert Systems with Applications, 42*(3), 990–1002.

Sahiner, B. S., Chan, H. P., Petrick, N., Helvie, M. A., & Goodsitt, M. M. (1998). Computerized characterization of masses on mammograms: The rubber band straightening transform and texture analysis. *Medical Physics, 25*(4), 516–526.

de Sampaio, W. B., Silva, A. C., de Paiva, A. C., & Gattass, M. (2015). Detection of masses in mammograms with adaption to breast density using genetic algorithm, phylogenetic trees, LBP and SVM. *Expert Systems with Applications, 42*(22), 8911–8928.

Soulard, R., & Carr, P. (2011). Quaternionic wavelets for texture classification. *Pattern Recognition Letters, 32*, 1669–1678.

Tai, S. C., Chen, Z. S., & Tsai, W. T. (2014). An automatic mass detection system in mammograms based on complex texture features. *IEEE Journal of Biomedical and Health Informatics, 18*(2), 618–627.

Tan, M., Pu, J., & Zheng, B. (2014). Optimization of breast mass classification using sequential forward floating selection (SFFS) and a support vector machine (SVM) model. *International Journal of Computer Assisted Radiology and Surgery, 9*(6), 1005–1020.

Tang, J., Rangayyan, R. M., Xu, J., Naqa, I. E., & Yang, Y. (2009). Computer-aided detection and diagnosis of breast cancer with mammography: Recent advances. *IEEE Transactions on Information Technology in Biomedicine, 13*(2), 236–251.

Tsochatzidis, L., Zagoris, K., Karahaliou, N. A. A., Costaridou, L., & Pratikakis, I. (2017). Computer-aided diagnosis of mammographic masses based on a supervised content-based image retrieval approach. *Pattern Recognition, 71*, 106–117.

Varela, C., Tahoces, P. G., Mendez, A. J., Souto, M., & Vidal, J. J. (2007). Computerized detection of breast masses in digitized mammograms. *Computers in Biology and Medicine, 37*, 214–226.

Xie, W., Li, Y., & Ma, Y. (2016). Breast mass classification in digital mammography based on extreme learning machine. *Neurocomputing, 173, Part 3*, 930–941.

Zyout, I., Czajkowska, J., & Grzegorzek, M. (2015). Multi-scale textural feature extraction and particle swarm optimization based model selection for false positive reduction in mammography. *Computerized Medical Imaging and Graphics, 46, Part 2*, 95–107. Information Technologies in Biomedicine